# Magnetite nanoparticles for medical MR imaging

**Nanotechnology has given scientists new tools for the development of advanced materials for the detection and diagnosis of disease. In particular, superparamagnetic iron oxide nanoparticles (SPIONs) have been extensively investigated as novel magnetic resonance imaging (MRI) contrast agents due to a combination of favorable superparamagnetic properties, biodegradability, and surface properties. This review discusses the basics of MR imaging, the origin of SPION's unique magnetic properties, recent developments in MRI acquisition methods for detection of SPIONs, synthesis and post-synthesis processes that improve SPION's imaging characteristics, and the outlook of the translational potential of SPIONs.**

**Zachary R. Stephen, Forrest M. Kievit, and Miqin Zhang***
*Department of Materials Science and Engineering, University of Washington, Seattle, WA 98195, USA*
**E-mail: mzhang@u.washington.edu*

**Magnetic resonance imaging (MRI) has become one of the most widely used and powerful tools for non-invasive clinical diagnosis due to its high soft tissue contrast, spatial resolution, and penetration depth[1]. In addition, images are acquired without the use of ionizing radiation or radiotracers that would cause unwanted harmful side-effects. A considerable amount of research in medical MR imaging is focused on the development of contrast agents that can provide better delineation between healthy and diseased tissue. Magnetic nanoparticles (MNPs) are a major class of nanoscale material currently under extensive development for improved diagnosis of a wide range of diseases, including cancer[2], cardiovascular disease[3], and neurological disease[4]. The nanoscale dimensions of MNPs give rise to unique magnetic properties and the ability to function on a cellular and molecular level[5]. It is the combination of these characteristics that make MNPs such promising contrast agents for MRI applications.**

Among the various MNPs under investigation, superparamagnetic iron oxide nanoparticles (SPIONs) have attracted considerable interest due to their excellent magnetic properties, biocompatibility[6] and biodegradability[7]. While the *in vivo* applications of many nanoparticle-based contrast agents are hampered by toxicity concerns, SPIONs of several formulations have been approved by the Food and Drug Administration (FDA) as MRI contrast agents. These include Lumiren® for bowel imaging[8], Feridex IV® for liver and spleen imaging[9], and Combidex® for lymph node metastases imaging[10]. Recent advances in this field have further improved the magnetic and physiochemical properties of SPIONs[11], broadening their potential clinical applications.

## MR and relaxation properties of SPIONs

### Principles of MRI contrast

MRI employs a strong magnetic field that aligns the magnetic moments of protons in a sample producing an equilibrium magnetization along


ISSN:1369 7021 © Elsevier Ltd 2011

the *z*-axis ($M_z$) with a magnitude of $M_0$. A radio frequency (RF) pulse, at a resonant frequency capable of transferring energy to protons, rotates their magnetic moments away from the *z*-axis, in phase, to an angle called the flip angle. The choice of flip angle depends on the imaging sequence applied, but it is generally the transverse plane (*xy*-plane), causing a net magnetization of $M_{xy}$. Upon removal of the RF, the magnetic moments of the protons relax to equilibrium[1,12]. The time required for the magnetic moments to relax to the equilibrium state, which is broadly termed the relaxation time, is tissue-dependent.

MRI contrast in soft tissue is due to differences in the proton density, spin-lattice relaxation time ($T_1$) and spin-spin relaxation time ($T_2$) of the protons. $T_1$ is the time constant of the exponential recovery process of $M_0$ along the *z*-axis after an RF pulse. Protons that relax rapidly (short $T_1$) recover full magnetization along the *z*-axis and produce high signal intensities. For protons that relax more slowly (long $T_1$), full magnetization is not recovered before subsequent RF pulses, and so they inherently produce less signal and result in the so-called saturation effect. $T_1$ weighted images illustrate anatomy well and are preferred when a clear image of the structure is required[12].

$T_2$ is the time constant of the exponential decay of the transverse magnetization ($M_{xy}$) after an RF pulse. $T_2$ is related to the amount of time for the precessing magnetic moments of protons to become randomly aligned in the *xy*-plane after an RF pulse, eventually resulting in a net magnetic moment of zero in the *xy*-plane. This dephasing process can be caused by a combination of local inhomogeneities in the magnetic field due to magnetic interactions of neighboring molecules and by macroscopic effects related to subtle variations in the external magnetic field. When the dephasing time accounts for both intrinsic molecular interactions and extrinsic magnetic field inhomogeneities it is termed $T_2$*, and the images produced are considered to be $T_2$* weighted. $T_2$ weighted images are produced by eliminating the dephasing effects caused by extrinsic magnetic field inhomogeneities and accounting for the molecular interactions alone. $T_2$ weighted images produce good pathological information since collections of abnormal fluid appear bright against the normal tissue background[1].

Spin-echo (SE) pulse sequences are used to eliminate external magnetic field effects and can generate $T_1$ or $T_2$ weighted images based purely on molecular interactions[1]. This signal eliminates extrinsic effects and provides quantitative $T_2$ data for $T_2$ weighted images. In its most basic form, the spin-echo scans employ two RF pulses with flip angles of 90° and 180° that produce a spin echo. The 180° pulse serves to refocus the transverse magnetization, cancelling dephasing effects caused by inhomogeneities in the local magnetic field. The time between the application of the 90° pulse and the peak of the echo signal is termed the echo time (TE). Both TE and the time between RF pulse repetitions (TR) are responsible for the type of image produced. $T_1$ weighted images are produced by selecting short TR (250 – 700 ms) and short TE (10 – 25 ms), while $T_2$ weighted images are produced by long TR (> 2000 ms) and long TE (> 60 ms)[13].

In most tissue, intrinsic variations of $T_1$ and $T_2$ are small and often exogenous materials are employed clinically to enhance the contrast between the tissue of interest and the surrounding tissue. While nearly all MRI contrast agents affect both $T_1$ and $T_2$, usually the effects of contrast agents are more pronounced for either $T_1$ or $T_2$, leading to the categorization of these probes as $T_1$ or $T_2$ contrast agents. $T_1$ contrast agents are used to increase signal intensity providing positive contrast enhancement in $T_1$ weighted images, whereas, $T_2$ contrast agents decrease signal intensity resulting in a negative contrast enhancement in $T_2$ weighted images. Currently, the most widely used clinical contrast agents are based on paramagnetic chelates of lanthanide metals such as gadolinium[14]. The presence of paramagnetic ions near water protons shortens their $T_1$ relaxation time through coordination with water molecules providing increased contrast. While gadolinium chelates are widely used, their short blood circulation times, poor detection sensitivity, and toxicity concerns have led to the continued development of SPIONs for $T_2$ contrast enhancement[15,16].

### Magnetic properties of SPIONs

The unique magnetic properties of SPIONs arise from a combination of their atomic composition, crystal structure, and size effects. Bulk iron oxide consists of both $Fe^{2+}$ and $Fe^{3+}$ atoms and exhibits ferromagnetic behavior. Large ferrimagnetic crystals of $Fe_3O_4$ are comprised of multiple magnetic domains that exhibit magnetic moments that are aligned within a domain, but between domains, magnetic moments are oriented in random directions[17]. Ferrimagnetic particles below a critical diameter consist of a single magnetic domain. The critical diameter, defined as the size at which domain boundaries are no longer energetically favorable, is highly dependent on the anisotropy of the particles, and varies for different materials[18-20]. For spherical magnetite iron oxide ($Fe_3O_4$) the critical diameter is approximately 70 – 150 nm[18,20,21]. When the diameter of spherical magnetite particles is reduced below approximately 20 nm[20], the thermal energy available at room temperature is greater than the magnetostatic energy well barrier. The magnetic dipole is free to fluctuate and as a consequence the particle acts like a paramagnetic $Fe^{(2+,3+)}$ atom. Since a nanoparticle comprises thousands of atoms it is described as superparamagnetic; it combines the high magnetization of bulk magnetite with the paramagnetic nature of Fe ions (Fig. 1).

## Effects of SPIONs on MRI contrast

SPIONs primarily act to alter $T_2$ values of the water protons surrounding the particle. When SPIONs present in tissue are subject to an external magnetic field the large magnetic moments of the particles align to create large heterogeneous field gradients through which water protons diffuse. The dipolar coupling between the magnetic moments of water protons and the magnetic moments of particles cause efficient spin dephasing and $T_2$ relaxation leading to a decrease in signal intensity[22]. The contrast provided by SPIONs in a $T_2$ weighted

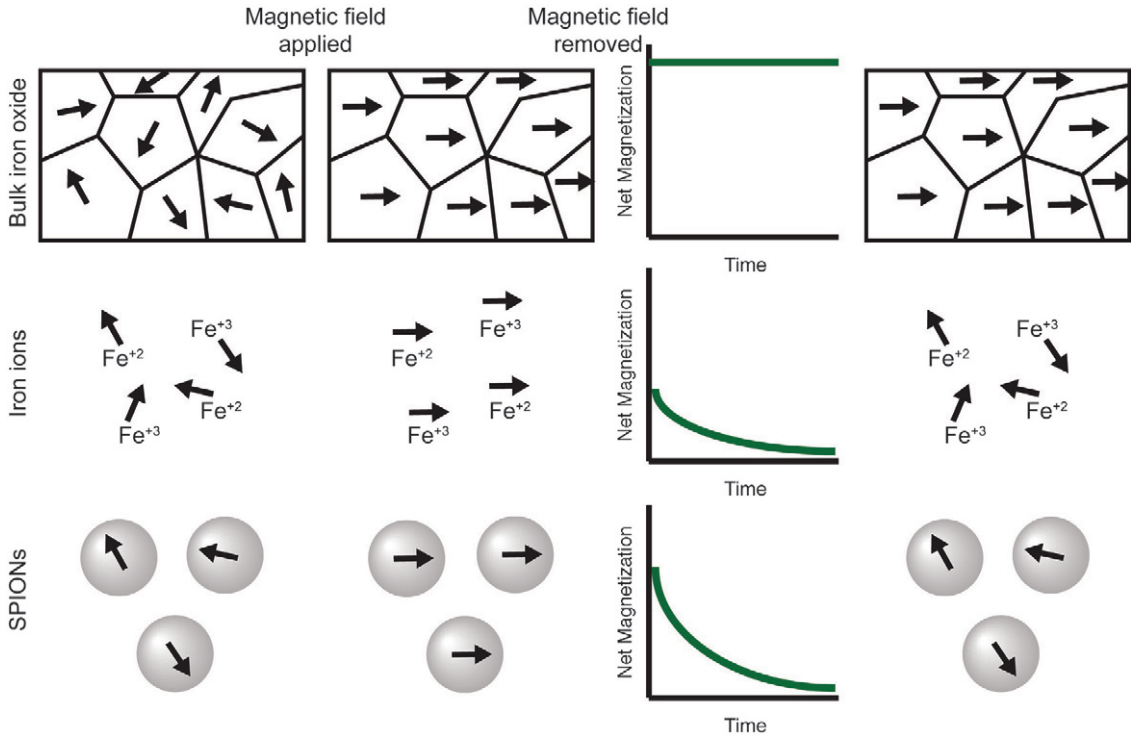


*Fig. 1 The effects of an external magnetic field on bulk magnetite (top), Fe ions (middle), and SPIONs (bottom). Before application of the magnetic field all magnetic moments are randomly aligned. Application of an external magnetic field aligns the moments along the z-axis of the magnetic field. The initial net magnetization of SPIONs is greater than Fe ions, but less than bulk magnetite. Upon removal of the magnetic field, the moments of bulk magnetite remain fixed along the z-axis while both Fe ions and SPIONs magnetic moments relax over time to equilibrium.*

image is termed negative contrast enhancement since areas with high concentrations of SPIONs appear dark on MR images.

While SPIONs provide efficient shortening of $T_2$ and generate excellent contrast enhancement in tissue with longer $T_2$ characteristics, signal loss due to the presence of SPIONs can make it difficult to distinguish contrast enhancement in low signal body regions[23,24]. Senpan *et al.* have recently reported a $T_1$ weighted colloidal cross-linked iron oxide nanoparticle comprised of oleate-coated magnetite particles within a cross-linked phospholipid nanoemulsion[25]. This formulation decreased $T_2$ effects and allowed positive $T_1$ weighted contrast detection at nanomolar concentrations. Additionally, ultrasmall superparamagnetic iron oxide (USPIO), i.e., SPIONs with core diameters less than 10 nm, are capable of producing positive contrast in $T_1$ weighted images[26,27]. While positive $T_1$ contrast is possible with USPIO, this benefit is at the expense of their $T_2$ effects[18,28].

Another approach that has recently been investigated is the addition of a gadolinium chelate on the polymer coating of SPIONs[29]. This dual contrast agent efficiently reduces both $T_1$ and $T_2$ relaxation times and achieves good contrast in mice for both $T_1$ and $T_2$ weighted images. This unique combination allows for the acquisition of both highly detailed $T_1$ weighted anatomical images and pathologically relevant $T_2$ weighted images with a single imaging nanoprobe. In addition, such a contrast probe could provide enhanced $T_1$ weighted imaging of brain tumors. Common clinical gadolinium chelates such as gadolinium diethylenetriamine penta-acetic acid (Gd-DTPA) cannot traverse the blood-brain barrier (BBB) without the use of invasive techniques[30,31], limiting their application in brain tumor imaging. A significant advantage of SPIONs is their relatively large surface area which allows for the efficient addition of biologically active moieties such as BBB-penetrating peptides for non-invasive brain tumor imaging. For example, Veiseh *et al.* have shown that SPIONs labeled with chlorotoxin (CTX) peptide, a targeting agent with high affinity for tumors of neuroectodermal origin through binding of the membrane-bound matrix metalloproteinase-2 complex, can pass the BBB and successfully target brain tumors in a transgenic mouse model[32-35]. The exclusion of Gd-DTPA from the parenchymal region signifies that the BBB is not compromised before or after the administration of CTX labeled SPIONs (Fig. 2), and highlights one advantage of SPIONs over commonly used Gd-chelates.

## MRI acquisition methods for improved SPION detection

The detectability of SPIONs *in vivo* can be improved through synthesis techniques that enrich their magnetic properties (further discussed under "Important SPION design parameters" below), and through enhanced MRI acquisition methods that improve SPION detection. Acquisition methods that achieve low detection limits will be essential as the next generation of SPIONs move toward clinical application.

Lower detection limits will allow for administration of lower SPION dosages while improving contrast. In addition to methods that improve the negative contrast enhancement inherent to traditional $T_2$ weighted methods, new techniques that generate positive contrast enhancements are currently being developed.

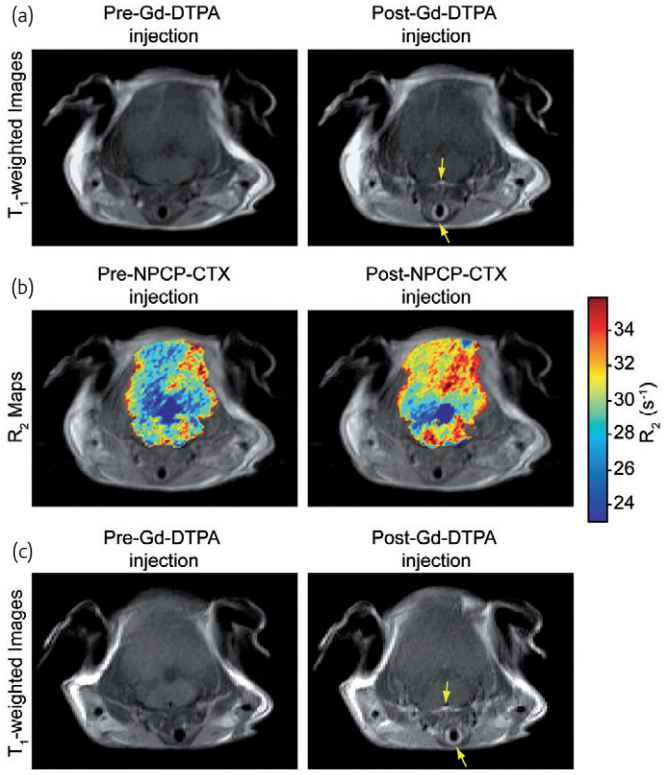


*Fig. 2 Comparison of the BBB permeating ability of Gd-DTPA and NPCP-CTX. (a) $T_1$ weighted MR images of N2:SmoA1 mice before and 5 min after the injection of Gd-DTPA. (b) colorized $R_2$ ($1/T_2$) maps superimposed onto proton density–weighted images obtained before and 48 h after the injection of NPCP-CTX. (c) $T_1$ weighted MR images of N2:SmoA1 mice before and 5 min after the injection of Gd-DTPA obtained 48 h after NPCP-CTX administration. Arrows indicate blood vessels. Reprinted with permission from[32], © 2010 American Association for Cancer Research.*

Historically, MRI acquisition methods for the detection of SPIONs have been based on $T_2$ weighted SE pulse sequences and $T_2$* weighted gradient echo (GRE) pulse sequences that give quantitative and qualitative information about the location of SPIONs *in vivo*, respectively[36-38]. Recently, an effort to improve detection limits has led to the modification of traditional SPION pulse sequences[37], as well as the application of nontraditional SPION pulse sequences such as fluid attenuated inversion-recovery (FLAIR)[39,40].

The sensitivity of MRI in the detection of single SPION loaded cells increases linearly with increasing resolution and increases hyperbolically with increasing signal-to-noise ratios (SNR)[37]. Based on this observation, imaging with both high resolution and high SNR would give the greatest SPION detection capabilities; however, increasing resolution and SNR, both of which increase image acquisition time, would result in unreasonably long acquisition times. Since there are diminishing returns in increasing SNR, reduction in voxel (volumetric pixel) size should be of primary concern to maintain acceptable imaging times. With this in mind, Hyen *et al.* used fast imaging employing a steady-state acquisition (FIESTA) sequence based on a GRE pulse sequence that was able to detect femtomole quantities of SPIONs in labeled single cells *in vitro*[37]. With this pulse sequence, images are weighted by a ratio of $T_2$ and $T_1$, and detection limits are comparable to those of positron emission tomography (PET)[41].

The fluid-attenuated inversion recovery (FLAIR) sequence was developed to nullify signals from fluid and has been shown to be useful in the diagnosis of central nervous system diseases[42]. This sequence first inverts the magnetic moments of protons in the *z*-axis before an additional 90° RF pulse at time TI (time between 180° and 90° RF pulse) tilts the magnetic moments into the *xy*-axis. This process can attenuate both tissue and/or fluid based on the chosen TI, but

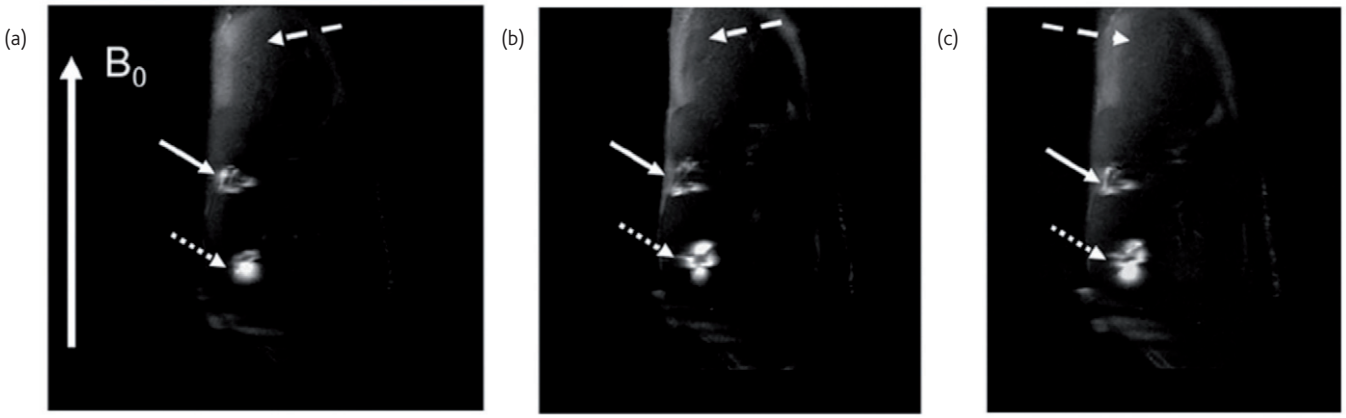


*Fig. 3 Signal variation among adjacent slices (a–c) from an in vivo 3T FSE 3D IRON acquisition obtained in an ischemic rabbit hindlimb with two injection sites of SPION-labeled stem cells (250 000 cells: dotted white arrow, 125 000 cells: solid white arrow). Excellent background suppression leads to clear visualization of the stem cell injection sites with positive contrast and a larger volume of hyperintense signals for the 250 000 cell injection site. The dashed white arrow indicates imperfections in both the on-resonant water suppression and off-resonant fat suppression. Reprinted with permission from[43]. © 2007 John Wiley & Sons.*

suffers from long imaging times. Fukukura *et al.* recently demonstrated the effectiveness of a more rapid FLAIR echo-planar imaging (FLAIR EPI) sequence[39,40] for the detection of malignant liver lesions with SPION contrast enhancement[42]. By suppressing signals from cysts, vascular structures, and periportal tissue, the FLAIR EPI sequence was more sensitive for the detection malignant liver tumors than either the $T_2$ weighted SE pulse sequences or the $T_2$* weighted GRE pulse sequences in human patients.

Limitations of $T_2$ contrast in low signal tissues have led to the development of specific pulse sequences that produce positive contrast in the presence of SPIONs. These methods attenuate the background signal so that only fluid and tissue immediately adjacent to SPIONs are visible in MR images (Fig. 3). The current positive contrast sequences are classified as selective RF pulse methods[43-45], dephased methods[46], and off-resonance methods[47]. Selective RF pulse methods, such as inversion-recovery with on-resonant water suppression (IRON), employ inversion of magnetization in conjunction with a spectrally-selective on-resonant saturation pre-pulse that only generates signal from off-resonant protons in close proximity to SPIONs. Dephased methods employ a slice gradient in the region near the SPION that dephase background signal protons, but conserve signal from protons surrounding the SPION due to their induced magnetic field. Off-resonance methods utilize spectrally selective RF pulses that excite and refocus the off-resonance water surrounding SPIONs, while suppressing on-resonance signals from surrounding tissue. In addition to positive contrast sequences, post-processing methods that do not require special sequences for acquisition of positive contrast images have been developed[48,49]. Liu *et al.* compared a post-processing susceptibility-gradient mapping (SGM) technique to IRON and the White Marker (dephased method) positive contrast sequences[50]. SGM more clearly delineates glioma tumors labeled with SPIONs than either the IRON or White Marker sequences in rats. Nevertheless, further studies are needed to compare the detection limit of the various positive contrast methods with those of the traditional spin echo methods.

## Important SPION design parameters

The magnetic properties of the SPION are affected by the crystallinity and size of the magnetite core. In addition, surface modifications including polymer coatings and tissue targeting agents can have a profound effect on the efficiency of SPIONs as MRI contrast agents. These modifications can increase local concentrations of SPIONs in the tissue of interest while decreasing the concentration in background tissue. The efficiency of these contrast agents to increase the rate of relaxation of surrounding protons can be expressed by the relaxivity ($r_1$, $r_2$), which is defined as the slope of the plot $1/T_1$ or $1/T_2$ as a function of SPION concentration. By carefully considering the parameters of core synthesis and post synthesis modifications, materials with superior relaxivity properties and *in vivo* kinetics can be produced.

### Core considerations

Synthesis methods of SPIONs have a dramatic effect on their crystallinity. The two most common methods are co-precipitation[51-53] and thermal decomposition[54,55]. Synthesis of SPIONs by co-precipitation of $Fe^{2+}$ and $Fe^{3+}$ in aqueous solutions has traditionally been the most utilized synthesis method[56]. This method typically results in a lack of well-defined nanocrystalline size, stoichiometry, and magnetism[28,57]. Furthermore, the production often yields both maghemite ($Fe_2O_3$) and magnetite. Magnetite is preferred of the two materials because of its superior magnetic properties[58]. Synthesis parameters of the co-precipitation method must be rigorously controlled so that nanocrystalline magnetite is the major product to maintain acceptable MR signal-enhancing effect. Thermal decomposition of iron organometallic compounds is a more recent approach that produces monocrystalline particles of stoichiometric magnetite[59]. The high temperatures of the thermal decomposition method allows for a higher rate of diffusion during the growth phase of the SPIONs resulting in improved magnetic properties that demonstrate high relaxivity.

The core size of SPIONs has significant effects on relaxivity properties. The thermal decomposition synthesis method produces SPIONs with highly controllable, monodisperse size distributions. Through minor modifications to synthesis parameters, SPIONs with mean diameters

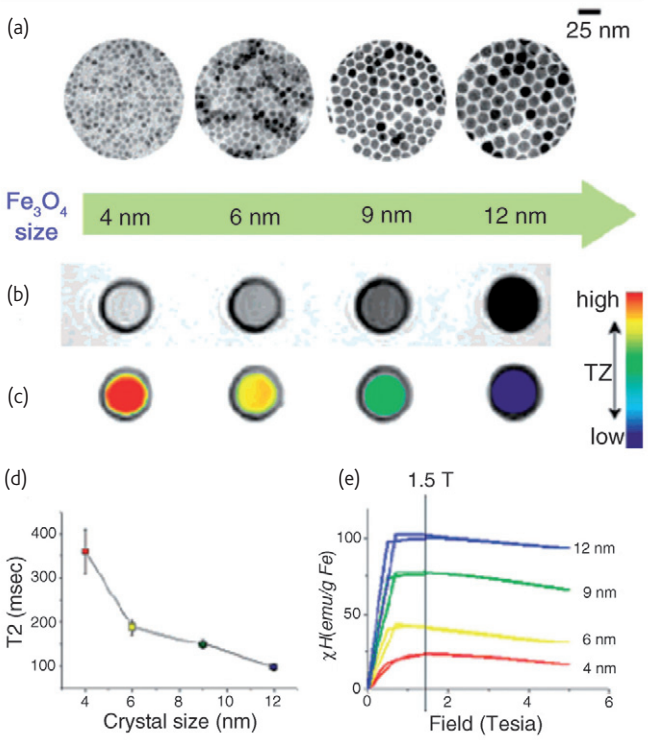


*Fig. 4 Nanoscale size effects of water soluble iron oxide nanocrystals on magnetism and induced MR signals. (a) TEM images of $Fe_3O_4$ nanocrystals of 4, 6, 9, and 12 nm. (b) Size dependent $T_2$ weighted MR images of nanocrystals in aqueous solution at 1.5 T. (c) Size dependent changes in color-coded MR images based on $T_2$ values. (d) Graph of $T_2$ value versus nanocrystal size. (e) Magnetization of nanocrystals measured by a SQUID magnetometer. Reprinted with permission from[28]. © 2005 American Chemical Society.*

ranging from 4 nm to 20 nm can be produced with a narrow size distribution[60]. Fig. 4 illustrates the correlation between particle size and $T_2$ relaxation due to changes in magnetic properties. As particle size is reduced there is a corresponding reduction in saturation magnetization which in turn reduces the $T_2$ relaxation capabilities of SPIONs. This phenomenon is a result of increased surface-to-volume ratios due to decreased particle diameter. As particle size is reduced, the percentage of atoms found on the particle surface increases and the curvature of the particle surface considerably increases, resulting in significant surface effects. The atoms on the surface have a reduction in nearest neighbors resulting in unsatisfied bonds, as well as noncollinear spins, spin canting, and spin-glass-like behavior. These effects can severely diminish the saturation magnetization of small SPIONs by reducing the number of atoms that contribute efficiently to the particle's magnetic moment[61].

## Surface modifications

### Surface coating

Passivation of the iron oxide core is necessary for successful application of SPIONs *in vivo*. The high surface-to-volume ratio of nanoparticles yields high surface energies, fascilitating surface oxidation which can have a significant effect on the magnetic properties of SPIONs[58,61,62]. In addition to surface oxidation, high surface energies can lead to particle aggregation or clustering in physiological environments[63]. Modification approaches for surface passivation of SPION cores generally provide a reduction in surface energy as well as either steric or electrostatic repulsion. Upon intravenous injection, SPIONs are subjected to protein adsorption, or opsonization, in the first step toward clearance from the blood stream by the reticuloendothelial system (RES). Evading RES uptake increases the blood half-life of SPIONs which is crucial for many MRI applications, as increased blood-circulation time maximizes the odds of SPIONs reaching their target tissue. A common technique to avoid opsonization and eventual clearance by the RES is to utilize hydrophilic coatings[64] such as poly(ethylene glycol) (PEG)[65] and zwitterionic[66] polymers that resist protein fouling.

Many materials and coating approaches have been utilized for modifying the surface of SPIONs. Polymers are the most widely used coating materials and can be classified as hydrophilic or amphiphilic, neutral or charged, homopolymers or copolymers[67,68]. These polymers can be anchored on the iron oxide surface by hydrogen bonds, electrostatic forces or through pseudo-covalent bonding[16]. In general, the coating should provide the SPION with a hydrophilic exterior to increase water solubility and stability.

The choice of coating material can have a significant effect on the relaxivity of SPIONs. The coordination chemistry of the inner capping ligand(s) and the hydrophilicity of the coating layer are important factors on particle relaxivity[62,69]. Daou *et al.* have shown that the coupling of surface coatings with the core of the SPION by carboxylates leads to spin canting and decreased net magnetization, yet this effect is not observed when coupling is performed with phosphonates[62]. Additionally, the use of hydrophilic molecules such as polyethylenimine (PEI) as capping ligands allows for greater hydration around the magnetic core and yields higher proton relaxivity than SPIONs capped with hydrophobic ligands such as oleic acid[69].

Polymer chain length, which corresponds to coating thickness, also has significant effects on relaxivity. Computer simulations have shown the effect of coating thickness on relaxivity is determined by two competing factors: the physical exclusion of protons from the SPION's magnetic field and the residence time for protons within the coating zone[70]. The structure of the coating layer determines which factor dominates. LeConte *et al.* studied the effects of chain length on relaxivity for SPIONs with a bilayer coating[70]. In this system, the inner hydrophobic layer excludes water, while the outer hydrophilic PEG layer allows for water diffusion in the coating zone. Increasing PEG chain length led to a reduction in $r_2$ values. Here it seems that the exclusion of water from the core by the inner hydrophobic layer more than offsets any effect caused by increasing the hydrophilic PEG layer thickness. Recent studies by Hu *et al.* have shown that when water molecules are not excluded from regions close to the SPION core, $r_2$ relaxivity is increased with increased chain length[71]. SPIONs with diameters of 3, 4, 5, and 6 nm were coated with a single polymer layer of either short chain diethylene glycol or long chain PEG. Modification with PEG leads to an increase from 29 to 47, 42 to 69, 48 to 86, and 61 to 119 $mM^{-1}s^{-1}$ for the four SPION diameters respectively. These differences can be attributed to a larger water-slow diffusion layer of PEG modified SPIONs. Measurements of water diffusion coefficients in solutions of PEG of varying molecular weights indicate that water moves more slowly in more highly concentrated PEG environments[72]. Protons in the slow water diffusion layer spend a longer period of time in close proximity to the magnetic field of the SPION core allowing for more efficient dephasing of the magnetic moments of neighboring protons.

### Targeting agents

Contrast agents that specifically target tissue can increase SNR by increasing local SPION concentration, potentially allowing for earlier detection of disease tissue such as small solid tumors and metastatic cells. Early SPIONs relied on passive targeting through the enhanced permeation and retention (EPR) effect which is the primary route for passive targeting in solid tumors. The EPR effect aids in nanoparticle uptake by way of leaky vasculature which allows particles with a hydrodynamic size generally less than 100 nm in diameter to cross from the vasculature into the interstitium[73,74]. Poor lymphatic drainage then aids in the entrapment of particles in solid tumors.

Alternatively, active targeting strategies provide mechanisms for the specific accumulation of contrast agents within diseased tissue or cells. These strategies are based on the targeting of unique molecular signatures of afflicted cells, such as over-expressed growth factors and

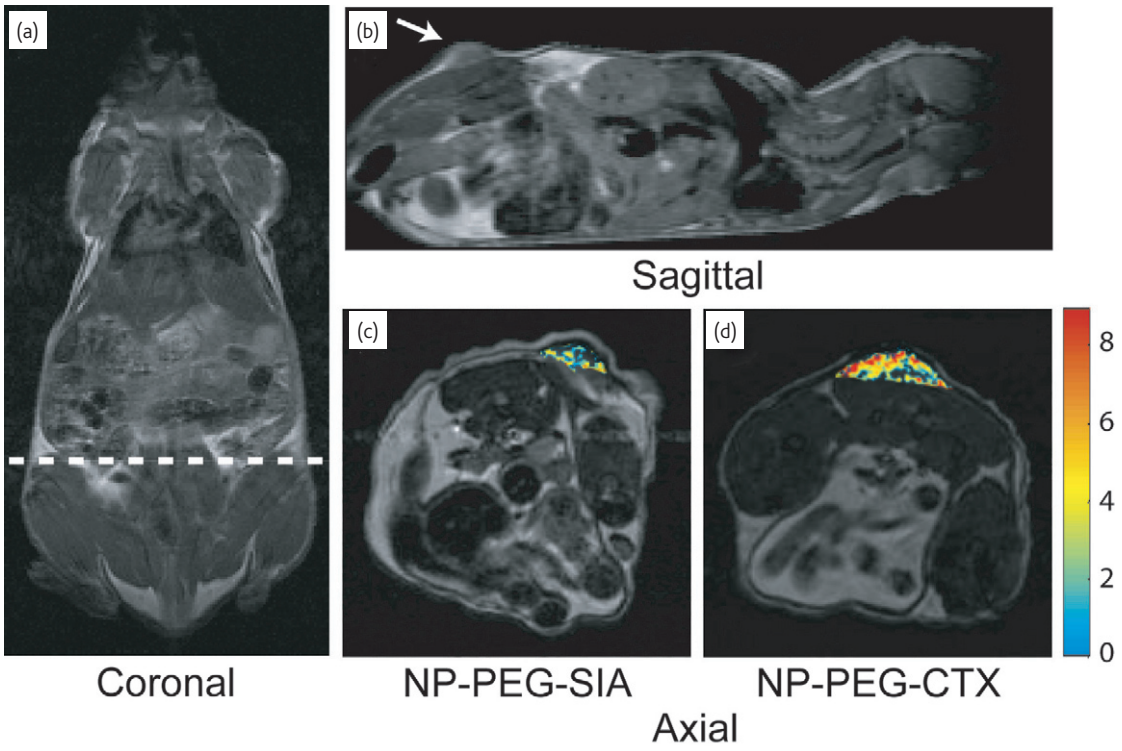


*Fig. 5 MR anatomical image of a mouse in the coronal plane. (a) The dotted line indicates the approximate location of the axial cross-sections displayed in (c) and (d). Anatomical image in the (b) sagittal plane displaying the location of the 9L xenograft tumor (white arrow). Change in $r_2$ relaxivity values for the tumor regions for a mouse receiving (c) non-targeting NP-PEG-SIA and (d) targeting NP-PEG-CTX 3h post-injection. Reprinted from[77]. © Wiley-VCH Verlag GmbH & Co. KGaA. Reproduced with permission.*

nutrient receptors[75]. Many types of ligands have been investigated in the targeting of these markers including antibodies, peptides, small molecules, and aptamers[76]. A recent study by Sun *et al.* illustrates the ability of targeting ligands to improve MR signal in diseased tissue[77]. In this study, PEG coated SPIONs were modified with CTX. Fig. 5 shows MR images that demonstrate tumor-specific SPION accumulation in tumors of a 9L xenograft mouse model. In a similar approach, Fang *et al.* modified SPIONs with either cyclic arginine-glycine-aspartic acid (RGD) which targets tumor endothelial cells, or CTX[78,79]. SPIONs modified with RGD (NP-RGD) or CTX (NP-CTX) show significant increases in $r_2$ values in tumors post injection in a xenograft U87-MG tumor mouse model, while non-targeted control SPIONs do not.

Active targeting is not only important for improving tissue targeting specificity, but has also been shown to improve the distribution of SPIONs within the targeted tissue. Improved distribution of SPIONs *in vivo* can be an important factor in maximizing relaxivity in tissue and cells. SPIONs tend to accumulate and even cluster in some specific tissue and/or cells, affecting their relaxation properties[80,81]. Transverse relaxivity first increases with increased cluster size followed by a marked decrease as cluster size continues to grow. Improved nanoparticle distribution in tissue due to active targeting has been demonstrated by several research groups[82-84]. In studies by Kievit *et al.*, SPIONs were modified with both DNA for gene therapy and CTX

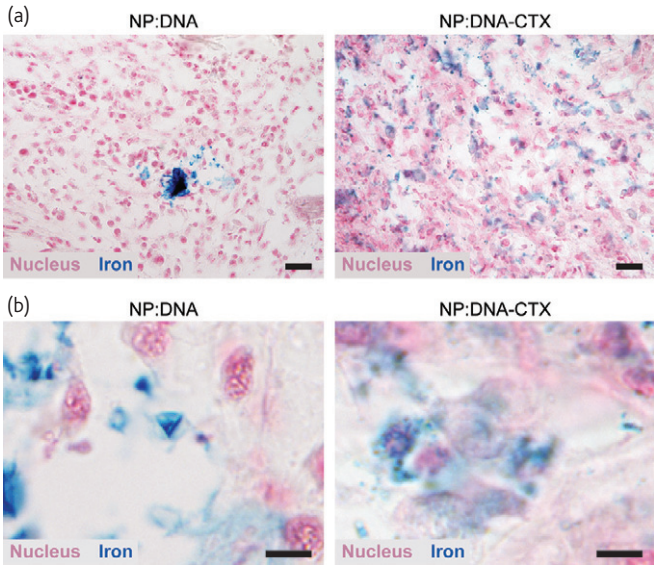


*Fig. 6 Histology analysis of C6 xenograft tumors showing NP distribution. (a) Prussian blue stained sections of tumors from mice treated with non-targeted (NP:DNA) and targeted (NP:DNA-CTX) nanovectors. The scale bar corresponds to 20 μm. (b) Images of Prussian blue stained sections at high magnification for better visualization of nanovector localization. The non-targeted NP:DNA treated tissue clearly shows more intense blue signals (indicating greater clustering) than the targeted NP:DNA-CTX treated tissue. The scale bar corresponds to 5 μm. Reprinted with permission from[82]. © 2010 American Chemical Society.*

(NP:DNA-CTX), with SPION/DNA as a non-targeted control (NP:DNA). Fig. 6 shows the reduction of SPION clustering in C6 tumors of a xenograft mouse model. The improved SPION distribution can act to minimize any reduction in relaxivity due to large cluster formation, leading to higher SNR and in turn, better delineation of tumor margins.

**Multimodal imaging**

SPIONs were specifically developed as an MR imaging contrast agent, yet advances in coating technologies have allowed for the addition of other functional imaging moieties including those for optical[32,85,86] (e.g., fluorophores) and nuclear imaging[83,87,88] (e.g., radionuclides). These multifunctional SPIONs can be designed to incorporate complementary imaging modalities that synergistically provide more accurate information *in vivo*. Each imaging modality has its advantages and limitations and no one modality can give a comprehensive snap shot of a biological system.

Fluorescent labeled SPIONs may serve as a platform for the next generation of multifunctional probes for multimodality imaging. They have been developed with the goal of providing optical contrast that will enable surgeons to intraoperatively distinguish cancer tissue from healthy tissue[32,85]. These nanoparticles provide fluorescence through the addition of numerous chromophores on the polymeric coating. SPIONs labeled with the near-infrared dye, Cy5.5, and CTX have shown the ability to produce both MRI and fluorescent tumor contrast in the brain of medulloblastoma transgenic mice (Fig. 7)[32]. Kumar *et al.* recently developed a SPION conjugated to Cy5.5 and myristoylated polyarginine peptides for translocation across the BBB[79]. This probe showed remarkable uptake by U87 human glioma cells *in vitro* and excellent delineation of stereotactically injected tumors *in vivo* by MRI. These advances in SPION design would allow for both preoperative MR imaging and intraoperative optical monitoring with a single imaging probe that could improve survival rates of brain tumor patients through better delineation of tumor boundaries.

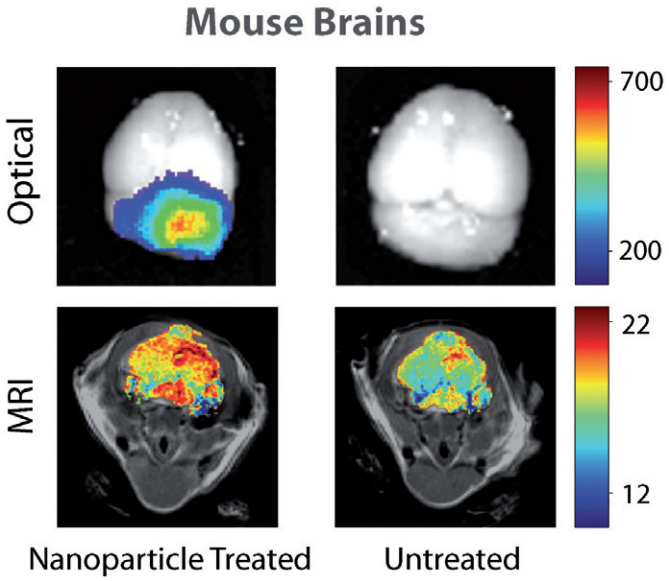


*Fig. 7 Ex vivo optical imaging and in vivo MR imaging of brain tumors from a mouse treated with Cy5.5 labeled SPIONs (left) and an untreated mouse (right). The optical spectrum gradient bar corresponds to increasing fluorescent intensity. The color gradient bar for MR images corresponds to increasing $r_2$ values. Adapted with permission from[32], © 2010 American Association for Cancer Research.*

PET/MRI multimodal imaging may offer significant advantages over either imaging modality alone. Several research groups have recently developed dual PET/MRI contrast probes that combine a SPION core with the radionuclide, Cu-64 chelated on the polymeric surface of the nanoparticle[83,87,88]. A combined PET/MRI contrast probe in an integrated system could obtain near perfect spatial registration of molecular/functional PET and anatomic/functional MRI[89,90]. This combination allows highly detailed anatomical MR images to be co-registered with PET images that currently have greater sensitivity to the location of contrast probes than clinical MRI[87]. While SPIONs with multimodal imaging capabilities have been developed, their full potential has yet to be realized due to a lack of integrated multimodal imaging instrumentation.

## Conclusions and outlook

SPIONs have been extensively studied as MRI contrast agents and several formulations have been approved for clinical use. However, their widespread utility has yet to be realized due to limitations of current detection limits and a lack of tissue specificity. Recent developments in both MRI acquisition methods and SPION synthesis and postsynthesis modifications have led to significant improvements in SPION detection sensitivity and *in vivo* bio-distribution. Beyond modifications to current MRI acquisition methods that demonstrate greater SPION sensitivity in $T_2$ weighted negative enhancement images, new acquisition methods are being developed that can provide positive contrast and potentially address current limitations of SPION contrast enhancement. These imaging techniques take advantage of the magnetic properties of SPIONs that are continually improving due to a better understanding of core synthesis parameters that affect both core crystallinity and size, as well as postsynthesis modifications that can have a dramatic effect on their magnetic properties and *in vivo* behavior. In addition, modifications of SPION surfaces with optical and nuclear imaging probes for multimodal imaging could improve diagnosis methods by combining the beneficial characteristics of each imaging modality.

The improvement of current detection limits is necessary for the successful translation of newly designed SPIONs to broad clinical application. Because of their magnetic properties and ease of functionalization, SPIONs have gained interest as theranostic agents capable of both providing diagnostic information and delivering therapeutics. In addition, the use of SPIONs for cell tracking in stem cell therapies has shown great promise. The potential of such applications in clinical settings is dependent on the development of highly sensitive imaging methods, as well as efficient contrast probes,

and will only be realized with improvements to current detection limits.

Despite recent improvements to imaging methods that exploit the magnetic properties of SPIONs, there is still a need to improve detection of these probes *in vivo*. Additional research is needed to both optimize methods for synthesis of highly reproducible monocrystalline SPIONs and to gain a better understanding of the effects of polymeric coatings on magnetic properties. By addressing these issues researchers can usher in the next generation of SPIONs for MR imaging. mt

## Acknowledgements

*We acknowledge the support of the NIH Grants R01CA134213, R01EB006043, and T32CA138312.*

### REFERENCES


1. Edelman, R. D., *et al.*, *MRI: Clinical Magnetic Resonance Imaging*. 2 ed.; W. B. Saunders Company: Philadelphia, Pennsylvania, 1996, pp. 1150.
2. Ferrari, M., *Nat Rev Cancer* (2005) **5**(3), 161.
3. Wickline, S. A., *et al.*, *J Magn Reson Imaging* (2007) **25**(4), 667.
4. Corot, C., *et al.*, *Invest Radiol* (2004) **39**(10), 619.
5. Sun, C., *et al.*, *Adv Drug Deliv Rev* (2008) **60**(11), 1252.
6. Sun, C. R., *et al.*, *Acs Nano* (2010) **4**(4), 2402.
7. Weissleder, R., *et al.*, *Am J Roentgenol* (1989) **152**(1), 167.
8. Wang, Y.-X., *et al.*, *Eur Radiol* (2001) **11**(11), 2319.
9. Bonnemain, B., *J Drug Target* (1998) **6**(3), 167.
10. Harisinghani, M. G., *et al.*, *New Engl J Med* (2003) **348**(25), 2491.
11. Veiseh, O., *et al.*, *Adv Drug Deliv Rev* (2010) **62**(3), 284
12. Berry, E., Bulpitt, A., *Fundamentals of MRI*. CRC Press: Boca Raton, 2009, pp. 298.
13. Westbrook, C., *et al.*, *MRI in Practice*. 3 ed.; Wiley-Blackwell: Hoboken, NJ, 2005, pp. 424.
14. Na, H. B., *et al.*, *Adv Mater* (2009) **21**(21), 2133.
15. Clarkson, R. B., *Blood-pool MRI contrast agents: Properties and characterization*. In *Contrast Agents I* (2002) Vol. 221, pp 201.
16. Terreno, E., *et al.*, *Chem Rev* (2010) **110**(5), 3019.
17. Bedanta, S., and Kleemann, W., *J Phys D: Appl Phys* (2009) **42**(1), 013001.
18. Gossuin, Y., *et al.*, *WIRE: Nanomed Nanobiotechnol* (2009) **1**(3), 299.
19. Mathew, D. S., and Juang, R.-S., *Chem Eng J* (2007) **129**(1-3), 51.
20. Krishnan, K., *IEEE T Magn* (2010) **46**(7), 2523.
21. Butler, R. F., and Banerjee, S. K., *J Geophys Res* (1975) **80**(29), 4049.
22. Holz, M., *Magn Reson Chem* (1993) **31**(13), S154.
23. Lipinski, M. J., *et al.*, *J Am Coll Cardiol* (2008) **52**(6), 492
24. Branca, R. T., *et al.*, *Proc Natl Acad Sci* (2010) **107**(8), 3693.
25. Senpan, A., *et al.*, *ACS Nano* (2009) **3**(12), 3917.
26. Park, J. Y., *et al.*, *Nanotechnology* (2008) **19**(36), 7.
27. Di Marco, M., *et al.*, *Int J Nanomed* (2007) **2**(4), 609.
28. Jun, Y.-w., *et al.*, *J Am Chem Soc* (2005) **127**(16), 5732.
29. Bae, K., *et al.*, *Bioconjugate Chem* (2010) **21**, 505.
30. Ding, D., *et al.*, *J Neuro-Oncol* (2010) **98**(1), 1.
31. Ding, D., *et al.*, *Neurol Res* (2010) **32**(8), 810.
32. Veiseh, O., *et al.*, *Cancer Res* (2009) **69**(15), 6200.
33. Sun, C., *et al.*, *Nanomed* (2008) **3**(4), 495.
34. Veiseh, O., *et al.*, *Biomaterials* (2010) **31**(31), 8032.
35. Veiseh, O., *et al.*, *Biomaterials* (2009) **30**(4), 649.
36. Moffat, B. A., *et al.*, *Mol Imaging* (2003) **2**(4), 324.
37. Heyn, C., *et al.*, *Magn Reson Med* (2005) **53**(2), 312.
38. Cole, A. J., *et al.*, *Biomaterials* (2010) **32**(8), 2183.
39. Moteki, T., and Sekine, T., *J Magn Reson Imag* (2004) **19**(1), 82.
40. Kumano, S., *et al.*, *Am J Roentgenol* (2003) **181**(5), 1335.
41. Phelps, M. E., *J Nucl Med* (2000) **41**(4), 661.
42. Fukukura, Y., *et al.*, *J Magn Reson Imag* (2010) **31**(3), 607.
43. Stuber, M., *et al.*, *Magn Reson Med* (2007) **58**(5), 1072.
44. Korosoglou, G., *et al.*, *J Am Coll Cardiol* (2008) **52**(6), 483.
45. Suzuki, Y., *et al.*, *Magn Reson Med* (2008) **60**(6), 1269.
46. Mani, V., *et al.*, *Magn Reson Med* (2006) **55**(1), 126.
47. Cunningham, C. H., *et al.*, *Magn Reson Med* (2005) **53**(5), 999.
48. Posse, S., *Magn Reson Med* (1992) **25**(1), 12.
49. Reichenbach, J. R., *et al.*, *J Magn Reson Imag* (1997) **7**(2), 266.
50. Liu, W., *et al.*, *NMR Biomed* (2008) **21**(3), 242.
51. Yoo, M. K., *et al.*, *J Nanosci Nanotechnol* (2008) **8**(10), 5196.
52. Forge, D., *et al.*, *J Phys Chem C* (2008) **112**(49), 19178.
53. Finotelli, P. V., *et al.*, *Braz J Chem Eng* (2008) **25**(4), 759.
54. Meledandri, C. J., *et al.*, *Langmuir* (2008) **24**(24), 14159.
55. Maity, D., *et al.*, *Funct Mater Lett* (2008) **1**(3), 189.
56. Gupta, A. K., and Gupta, M., *Biomaterials* (2005) **26**(18), 3995.
57. Sjögren, C. E., *et al.*, *Magn Reson Imag* (1997) **15**(1), 55.
58. Nedkov, I., *et al.*, *J Magn Magn Mater* (2006) **300**(2), 358.
59. Park, J., *et al.*, *Nat Mater* (2004) **3**(12), 891.
60. Sun, S., *et al.*, *J Am Chem Soc* (2003) **126**(1), 273.
61. Lu, A.-H., *et al.*, *Angew Chem Int Edit* (2007) **46**(8), 1222.
62. Daou, T. J., *et al.*, *Chem Mat* (2008) **20**(18), 5869.
63. Zhang, Y., *et al.*, *Biomed Microdevices* (2004) **6**(1), 33.
64. Berry, C. C., and Curtis, A. S. G., *J Phys D: Appl Phys* (2003) **36**(13), R198.
65. Otsuka, H., *et al.*, *Adv Drug Deliv Rev* (2003) **55**(3), 403.
66. Jia, G. W., *et al.*, *Langmuir* (2009) **25**(5), 3196.
67. Fang, C., and Zhang, M. Q., *J Mater Chem* (2009) **19**(35), 6258.
68. Fang, C., *et al.*, *Small* (2009) **5**(14), 1637.
69. Duan, H., *et al.*, *J Phys Chem C* (2008) **112**(22), 8127.
70. LaConte, L. E. W., *et al.*, *J Magn Reson Imag* (2007) **26**(6), 1634.
71. Hu, F., *et al.*, *Nanoscale* (2010) **2**(10), 1884.
72. Vergara, A., *et al.*, *Phys Chem Chem Phys* (1999) **1**(23), 5377.
73. Longmire, M., *et al.*, *Nanomedicine* (2008) **3**(5), 703.
74. Kievit, F. M., *et al.*, *Adv Funct Mater* (2009) **19**(14), 2244.
75. Sunderland, C. J., *et al.*, *Drug Develop Res* (2006) **67**(1), 70.
76. Alexis, F., *et al.*, *Urol Oncol* (2008) **26**(1), 74.
77. Sun, C., *et al.*, *Small* (2008) **4**(3), 372.
78. Fang, C., *et al.*, *Nanomedicine* (2010) **5**(9), 1357.
79. Kumar, M., *et al.*, *Magn Reson Med* (2010) **63**(3), 617
80. Larsen, B., *et al.*, *Nanotechnology* (2008) **19**(26), 265102.
81. Roch, A., *et al.*, *J Magn Magn Mater* (2005) **293**(1), 532.
82. Kievit, F. M., *et al.*, *ACS Nano* (2010) **4**(8), 4587.
83. Bartlett, D. W., *et al.*, *Proc Natl Acad Sci USA* (2007) **104**(39), 15549.
84. Choi, C. H. J., *et al.*, *Proc Natl Acad Sci* (2010) **107**(3), 1235.
85. Veiseh, O., *et al.*, *Nano Lett* (2005) **5**(6), 1003.
86. Lee, M. J. E., *et al.*, *PLoS One* (2010) **5**(3), 8.
87. Lee, H. Y., *et al.*, *J Nucl Med* (2008) **49**(8), 1371.
88. Xie, J., *et al.*, *Biomaterials* (2010) **31**(11), 3016.
89. Cizek, J., *et al.*, *Neuroimage* (2004) **22**(1), 434.
90. Myers, R., *Brit J Radiol* (2002) **75**, S31.